Protein-Protein Interaction Investigated by Steered Molecular Dynamics: The TCR-pMHC Complex

Michel A. Cuendet* and Olivier Michielin*†‡
*Swiss Institute of Bioinformatics, Lausanne, Switzerland; †Ludwig Institute for Cancer Research, Lausanne, Switzerland; and ‡Multidisciplinary Oncology Center, Centre Hospitalier Universitaire Vaudois, Lausanne, Switzerland

ABSTRACT We present a novel steered molecular dynamics scheme to induce the dissociation of large protein-protein complexes. We apply this scheme to study the interaction of a T cell receptor (TCR) with a major histocompatibility complex (MHC) presenting a peptide (p). Two TCR-pMHC complexes are considered, which only differ by the mutation of a single amino acid on the peptide; one is a strong agonist that produces T cell activation in vivo, while the other is an antagonist. We investigate the interaction mechanism from a large number of unbinding trajectories by analyzing van der Waals and electrostatic interactions and by computing energy changes in proteins and solvent. In addition, dissociation potentials of mean force are calculated with the Jarzynski identity, using an averaging method developed for our steering scheme. We analyze the convergence of the Jarzynski exponential average, which is hampered by the large amount of dissipative work involved and the complexity of the system. The resulting dissociation free energies largely underestimate experimental values, but the simulations are able to clearly differentiate between wild-type and mutated TCR-pMHC and give insights into the dissociation mechanism.

INTRODUCTION

Recognition by the CD8+ T cell receptor (TCR) of antigenic peptides (p) presented by the major histocompatibility complex (MHC) class I molecules is the key step leading to T cell activation and, ultimately, target cell killing. The molecular events taking place at the TCR-pMHC interface are, therefore, subject of active research (see review in (1)). This system is of great interest for medical applications and, in particular, for cancer immunotherapy. The activity of the T cell in cytotoxic assays was shown (2,3) to depend on the affinity of the TCR for the pMHC complex. Furthermore, TCR binding and unbinding kinetic constants also proved to be key factors of cytotoxicity (4–7). In the prospect of optimizing TCR sequences that can be genetically incorporated into patient's lymphocytes and confer tumor immunity (8,9), there is a strong need for techniques to characterize quantitatively the thermodynamic and kinetic behavior of any given TCR in association with any peptide and any MHC. In addition to the computation of global properties, molecular dynamics (MD) simulations allow us to dissect details of the interaction at the atomic level, giving valuable insights into the molecular basis of TCR recognition, and guiding peptide or TCR rational design.

The TCR-pMHC studied here is the human A6 TCR, specific for the HTLV-1 virus Tax nonapeptide (LLFGYPVYV) bound to the HLA-A0201 MHC. The complex is shown in Fig. 1 *a*, in the bound and unbound states. Recognition of pMHC is mediated by the very specific complementarity determining region (CDR) loops (10) of the TCR. The Tax peptide is a strong agonist, i.e., it induces T cell activation at very low concentrations. The recognition mechanism is extremely sensitive, since a single mutation on the Tax peptide can turn it into a weak antagonist, which inhibits the T cell function instead of triggering it.

The A6/Tax/HLA-A0201 system was chosen because it has been extensively studied experimentally, together with four peptide mutants. In addition to x-ray structures (11,12), experimental data on T cell activation response, binding affinities, and kinetic constants are available for the Tax peptide and the mutants (see below). In this work, we focus on the Tax wild-type and the P6A mutant, in which the proline residue in the sixth position is replaced by an alanine. This mutation, shown in Fig. 1 *b*, induces minute changes in the crystal structures of the complexes. No contact between the mutated proline residue and the TCR is apparent in the x-ray structure. The only significant structural difference between the TCR-pMHC structures with the wild-type or the P6A-substituted Tax peptide is a packing defect consisting of an enlarged cavity partially filled with a bound water molecule (12). However, the mutation is able to change the peptide from a strong agonist to an antagonist, as revealed by cytotoxicity assays (12).

The P6A mutation has also an effect on the TCR binding thermodynamics. Equilibrium constants from sedimentation equilibrium analytical ultracentrifugation (13) correspond to free energy differences ΔG from bound to unbound TCR-pMHC of 34.5 kJ mol^{-1} for Tax and 22.6 kJ mol^{-1} for P6A. Early steady-state surface plasmon resonance (SPR) experiments (12) yielded a similar value for the Tax complex, $\Delta G =$ 34.7 kJ mol^{-1}. Two subsequent studies with the same method (14,15) implied a lower ΔG of 32.5 kJ mol^{-1}. A later experiment gave $\Delta G = 32.18$ kJ mol^{-1} (16). A recent study (17) using isothermal titration calorimetry showed the influence of pH and buffer on the binding thermodynamics and

Submitted February 15, 2008, and accepted for publication June 17, 2008.

Address reprint requests to Olivier Michielin, E-mail: olivier.michielin@isb-sib.cn.

Editor: Kathleen B. Hall.

0006-3495/08/10/3575/16 $2.00

doi: 10.1529/biophysj.108.131383

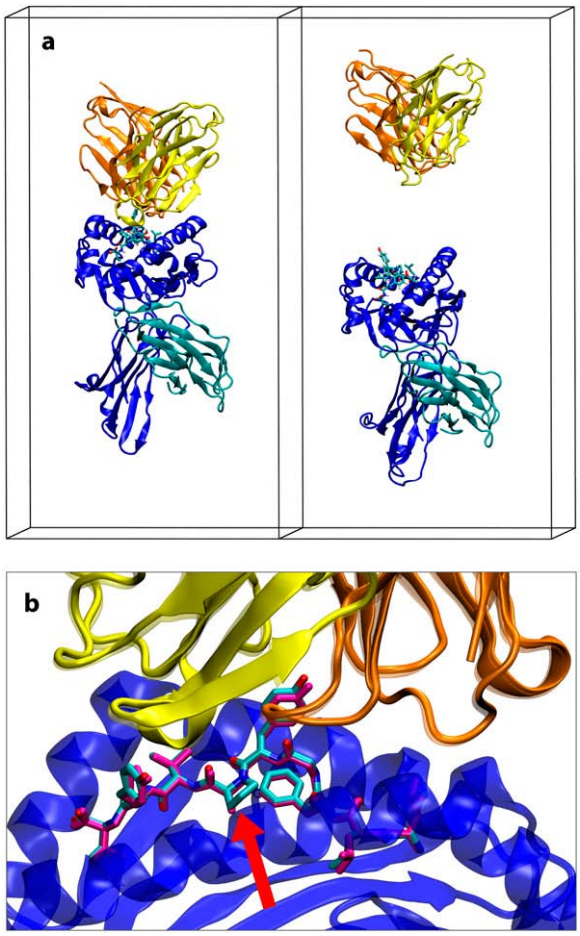

FIGURE 1 (*a*) Structure of the TCR-pMHC system studied here (A6/Tax/HLA-A0201). (*Left panel*) Bound state at the beginning of the simulation. (*Right panel*) Unbound state at the end of an individual pulling trajectory. The V_α and V_β chains of the TCR are represented in yellow and orange. The α-chain of the MHC is in dark blue and the β2-microglobulin domain of the MHC is in light blue. The Tax peptide is shown in stick representation. The lines represent the periodic simulation box and water molecules are omitted for clarity. The entire system comprises 84,238 atoms. (*b*) Comparison of the TCR-pMHC interface in crystal structures of the Tax complex or the P6A complex. All color codes are similar to panel *a* and the P6A peptide is drawn in pink. The red arrow shows the position of the mutation. The α-chains of the MHC were superimposed and, as the structures are almost indistinguishable, only the MHC of the tax complex is shown. The slightly different structure of the TCR in the P6A complex is shown with transparent material of same color as in the Tax complex.

yielded a ΔG of 39.2 kJ mol^{-1} for the Tax complex (for the same conditions as the SPR experiments). In addition, the latter study evidenced the role of protonation in the binding process, with 0.28 protons released to the buffer upon binding of A6 to Tax/HLA-A2 (at pH 7.4). Armstrong and Baker (17) derived an intrinsic ΔG of 38.5 kJ mol^{-1}, independent of protonation effects. We see that the experimental determination of ΔG still suffers some uncertainty, which probably also projects on the experimental values available to characterize the free energy barrier.

Binding and unbinding rate constants derived from kinetic SPR experiments (12) on the Tax complex indicate a free energy barrier with $\Delta G_{\text{off}} = 79.5$ kJ mol^{-1} and $\Delta G_{\text{on}} = 44.5$ kJ mol^{-1}, implying a ΔG of 35 kJ mol^{-1}, which is consistent with the above ΔG values. These activation free energies were calculated using simple transition state theory with no transmission coefficient, which gives reasonable agreement with other measurements not based on rate constants. These include a van 't Hoff analysis of the temperature dependence of ΔG values from SPR which led to $\Delta G_{\text{off}} = 78.3$ kJ mol^{-1} and $\Delta G_{\text{on}} = 46.6$ kJ mol^{-1} (15) and an experiment based on urea concentration variations, which gave $\Delta G_{\text{off}} = 78.66$ kJ mol^{-1} (16). The kinetic constants for the P6A complex could not be measured, but it is suspected that the free energy barrier is significantly lower (12).

The typical half-life of a TCR-pMHC complex is on the order of seconds (18,19), a timescale currently out of reach of standard MD simulations. Indirect methods have been used to compute relative free energy differences between bound TCR-pMHC complexes with peptides mutants (20). These methods take advantage of Hess' law on the binding/mutation thermodynamic cycle, and use thermodynamic integration to calculate the mutation free energy in the bound and unbound states. On the other hand, when the entire dissociation potential of mean force (PMF) is wanted, various MD methods are available to circumvent the timescale limitation. Standard methods rely on series of equilibrium simulations restrained or constrained at different fixed positions along the reaction coordinate. A recent class of methods rely on nonequilibrium dynamics, where the motion along the reaction coordinate is progressively driven by an external potential. These methods include the early targeted MD (21) and steered molecular dynamics (SMD) (22–24), which we use in this study.

We now briefly review the general framework of SMD. Our goal is to study the transition from state A (bound) to state B (unbound) along a reaction coordinate ξ (e.g., distance between proteins), with a free energy barrier of several times k_BT. The probability of observing a spontaneous barrier-crossing event within a reasonable simulation time is extremely low. To overcome this, a time-dependent external potential energy function u is applied to the physical system to drive the reaction from A to B. The physical system, described by the Hamiltonian $H_0(\mathbf{q},\mathbf{p})$, is called the intrinsic system. The perturbed system, called the extended or composite system (23,25), is described by the extended Hamiltonian

$$H(\mathbf{r},\mathbf{p},\xi_0(t)) = H_0(\mathbf{r},\mathbf{p}) + u(\mathbf{r},\xi_0(t)). \quad (1)$$

Here, $\xi_0(t)$ is a pure function of time used to drive the simulation such that the system is restrained in state A at time 0, and in state B at time τ. We denote $u(\mathbf{r}, t) = u(\mathbf{r}, \xi_0(t))$. If the reaction coordinate $\xi(\mathbf{r})$ is a function of atom positions, $u(\xi(\mathbf{r}), t)$ is called a steering function. The steering function is generally chosen harmonic and centered on a given reference reaction coordinate $\xi_0(t)$,

$$u(\mathbf{r},t)=\frac{k}{2}(\xi(\mathbf{r})-\xi_0(t))^2. \quad (2)$$

Other forms of steering function are possible, as will be described later. The reference reaction coordinate $\xi_0(t)$ is changed typically with a constant velocity, $\xi_0(t)=\xi_A+v_\xi t$. The harmonic constant k and the steering velocity v_ξ are parameters of the simulation. As $\xi_0(t)$ is varied, dissipative work is performed on the system, and a thermostat is used to couple the system to a heat bath which absorbs the excess heat.

SMD has been applied to a variety of biological systems in the last decade (26,27). First, ligand unbinding from a receptor was studied (22), followed by protein unfolding (28), as well as protein-protein interaction (29). Most of the early SMD studies were meant to reproduce atomic force microscope (AFM) experiments and were aimed at characterizing dissociation mechanisms or calculating rupture forces.

Recent advances in statistical mechanics, however, opened the possibility of recovering equilibrium free energy differences from SMD simulations. In such a nonequilibrium process, the external work done on the system from time 0 to τ is defined as

$$W(\tau)=\int_0^\tau dt\frac{\partial H}{\partial t}(\mathbf{r},\mathbf{p},\xi_0(t))=\int_0^\tau dt\frac{\partial u}{\partial t}(\mathbf{r},t). \quad (3)$$

Here, $W(\tau)$ represents the work accumulated by the composite system (as opposed to the work transferred from the perturbation potential to the intrinsic system (25)). In a nonequilibrium process, the work $W(\tau)$ is dependent on the path of the induced state transition, and thus on the initial condition at time 0. The second law of thermodynamics states that the average work recorded over many realizations of the process cannot be smaller than the difference of free energies between the initial and the final states, $\Delta G\leq\langle W\rangle$. Equality holds only if the process is quasistatic or reversible, in which case the work is independent of the path. A more general result, the Jarzynski identity (JI) (30), holds regardless of the speed of the process

$$e^{-\beta\Delta G}=\langle e^{-\beta W}\rangle_0, \quad (4)$$

where $\beta=1/k_BT$. The average $\langle.\rangle_0$ is taken over different trajectories with independent canonically distributed initial conditions. A strong requirement is to have a sufficiently large collection of trajectories to allow an accurate estimation of the exponential average in Eq. 4. This is a major concern for practical applications, as shown in several studies (31–34) assessing the practical efficiency of the method.

The JI was first reported (30) in 1997, and proved to apply to a variety of Hamiltonian and non-Hamiltonian dynamics (35), Markov-chain dynamics (36), or Langevin evolution (25). The relation with the transient fluctuation theorem (37) was elucidated by Crooks (36) for stochastic systems and Jarzynksi (38) and Evans (39) for deterministic systems. An alternative derivation of Eq. 4 using path integrals and the Feynman-Kac theorem was proposed by Hummer and Szabo (23). Park and Schulten (24) also demonstrated explicitly that the relation holds for the Gibbs free energy in an isothermal-isobaric ensemble. Recently the JI was derived (40–42) directly from the specific equations of motion used in thermostated and barostated MD. Liphardt et al. (43) showed the relevance of the JI to experimental data from forced unfolding of single RNA strands. The JI was applied as well to SMD simulations of systems such as transport through membrane channels (44), peptide unfolding (45,46), and ligand binding (47).

In the next section, Methods, we introduce the individual pulling scheme to properly actuate the dissociation of a large protein complex such as TCR-pMHC. We then present an appropriate postprocessing method to exploit the work recorded in individual pulling simulations with the JI to estimate the PMF of unbinding. A detailed description of the simulations performed concludes the section.

In Results and Discussion, simulation results for both the Tax peptide and the P6A mutant are discussed. We report 576 explicit solvent dedocking trajectories of 4 ns each, which represent a total of ~2.3 μs of simulation time, not including equilibration runs and preliminary trials. The large number of trajectories at hand provides enough statistics to extract relevant behavior of energetic observables of the system. On the one hand, the usually large fluctuations can be averaged out. On the other hand, the results are independent of the particularities related to an initial given condition, and thus become reliable in the statistical mechanical sense. Thanks to this approach, the interactions between TCR and pMHC along the reaction coordinate can be analyzed in terms of van der Waals and electrostatic energies. Exploiting the same averaging capabilities, global energy changes upon dissociation are monitored, including solvent-protein and solvent-solvent contributions. Taken together, these results obtained from a very large MD data set give new insights into the molecular recognition mechanisms that govern the TCR-pMHC association. Global energy components are presented here while single residue contributions together with hydrogen bonding and hydrophobic contact patterns will be discussed elsewhere (M. A. Cuendet, V. Zoete, and O. Michielin, in preparation).

We finally present the PMF results with an investigation of the convergence difficulties encountered with the Jarzynski method. The example of the TCR-pMHC complex provides a useful landmark for the general characterization of the applicability domain of the Jarzynski method.

METHODS

Individual pulling

Special care has to be taken in the choice of the form of the steering function, Eq. 2, and the choice of atoms to which it applies. Pulling of molecules is usually done by applying a force on one single atom (26,27,29) to mimic an

AFM experiment, in which case ξ is the distance between the pulled atom and a fixed atom. Another way is to define ξ as the distance between the center of mass (CM) of a protein and the CM of a ligand, which amounts to applying uniformly to each atom in the molecules a force proportional to its mass.

For big proteins with a rather loose structure and bound by a strong interaction, such as the TCR-pMHC complex, these approaches are not appropriate. On such a system, a single point force or a mass weighted uniform force can induce stretching of the proteins with tertiary structure distortions and partial unfolding before unbinding occurs, as illustrated in Fig. 2 *a*. Such large conformational changes are likely to be only artifacts of fast pulling, because the timescales required for a partial protein unfolding during free unbinding are not consistent with experimental dissociation rates. Moreover, in the case of the TCR-pMHC system, the structures of both MHC and TCR in solution are known to be similar to those in the bound state (18), except for the CDR regions and the peptide.

Additional problems arise during standard steered unbinding if the interaction between the proteins is spread over a large surface perpendicular to the pulling direction. If, during the pulling, one side of the interface unbinds while the other side remains bound, a force moment appears with respect to the CM. This results in a rotation of the proteins, which roll on each other instead of separating (see Fig. 2 *b*). These hinge opening or rolling types of pathways are considered unlikely for the TCR-pMHC system for three reasons. First, there is evidence that the TCR-pMHC interaction actually happens between closely packed multimers in vivo (49). Second, both TCR and MHC parts are attached to two parallel membranes, which prevent large rotatory movements. Third, our preliminary studies showed that unbinding with rolling requires a lot more external work than straight unbinding, which makes the trajectories with rolling much less likely in a Boltzmann sense.

To avoid the stretching and rolling artifacts, we introduce a new scheme to actuate the dissociation, which we call individual pulling. The individual pulling scheme, schematized in Fig. 2 *c*, proceeds as follows: in an average structure of the bound complex, the reference position of an atom is determined with respect to the CM of its respective unit (TCR or pMHC). A harmonic potential energy term centered on this reference position is then applied to the z coordinate of the atom, while lateral movements remain completely free. This amounts to a restraint on the root mean-square deviation (RMSD) along z in each unit. To achieve pulling, the reference positions of all restrained atoms are shifted uniformly along the z axis, each unit in opposite direction. During this process, the reference structures remain unchanged in each part, while the CM distance is increased. This scheme prevents big artifactual changes in the tertiary structure of each unit by distributing the pulling forces where reaction forces are strongest. In addition, this keeps the system well aligned during the unbinding, which is useful in an elongated simulation box.

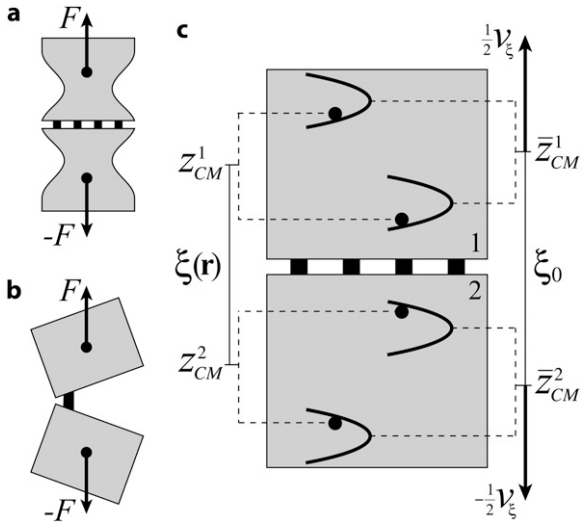

FIGURE 2 Scenarios for steered unbinding of two proteins: (*a*) Protein stretching or unfolding. (*b*) Rolling type of unbinding. (*c*) The individual pulling scheme. Black dots represent selected atoms in the protein, and the small parabolas represent the individual steering potential energy functions. See text for definitions of symbols.

Using individual pulling amounts to making a strong assumption on the reaction pathway. As we argued above, these assumptions are justified for the TCR-pMHC system. In addition, attention has to be paid not to restrain motions that are essential for protein function. In this study, only backbone and C_α atoms are subjected to a steering function, while side chains are left unrestrained. Unlike most of the TCR and MHC structure, the peptide and the CDR loops are known to be very flexible (50), and are therefore left completely unrestrained in our simulations. See the Simulation Setup section for details.

We now formally define the individual pulling scheme (see Fig. 2 *c*). Let the instantaneous reaction coordinate $\xi(\mathbf{r})$ be the actual distance along z between the CMs of the two units, located at z^1_{CM} and z^2_{CM} at time t,

$$\xi(\mathbf{r}) = |z^2_{\mathrm{CM}} - z^1_{\mathrm{CM}}|. \tag{5}$$

The corresponding driving parameter ξ_0 sets the reference distance between two hypothetical positions of the CMs, $\bar{z}^1_{\mathrm{CM}}$ and $\bar{z}^2_{\mathrm{CM}}$,

$$\xi_0 = |\bar{z}^2_{\mathrm{CM}} - \bar{z}^1_{\mathrm{CM}}|. \tag{6}$$

For each unit $j = 1, 2$, the reference structure determined before the pulling is expressed as a set of internal coordinates $\{\bar{\zeta}^j_i\}_{i=1}^N$. Each $\bar{\zeta}^j_i$ denotes the reference distance (along the z axis) of atom i to the reference position $\bar{z}^j_{\mathrm{CM}}$ of the CM of unit j. The $\{\bar{\zeta}^j_i\}$ are constant during the entire pulling experiment, and define the reference position $\bar{z}_i$ of atom i,

$$\bar{z}_i = \bar{z}^j_{\mathrm{CM}} + \bar{\zeta}^j_i. \tag{7}$$

The individual restraint of atom i is then defined as

$$u_i(z_i, t) = \frac{k_i}{2}(z_i - \bar{z}_i(t))^2. \tag{8}$$

The individual force constant k_i is defined such that two requirements are met. First, the sum of all individual forces $f_i = -k_i(z_i - \bar{z}_i)$ in each unit satisfies the action-reaction principle along the z axis,

$$\sum_{i\in\mathrm{unit1}} f_i = -\sum_{i\in\mathrm{unit2}} f_i. \tag{9}$$

Second, we want that the total CM perturbation energy in each unit resulting from all individual restraints is equivalent to a standard steering potential energy,

$$u_{\mathrm{CM}}(\xi(\mathbf{r}), \xi_0) = \frac{k_{\mathrm{CM}}}{2}(\xi(\mathbf{r}) - \xi_0)^2, \tag{10}$$

where k_{CM} is the equivalent harmonic constant driving the reaction coordinate. In this way, the individual pulling scheme can easily be compared to standard SMD acting on the CM. These two requirements are uniquely met by setting

$$k^j_i = \frac{m_i}{M_j} k_{\mathrm{CM}}, \tag{11}$$

with M_j the mass of unit j. With this choice of k^j_i, the sum of the internal forces vanishes in each unit.

During the simulation, $\xi_0(t)$ and the system's instantaneous reaction coordinate $\xi(\mathbf{r})$ set the overall steering force f_{CM}. For a given f_{CM}, which depends only on distances, we have to determine the individual forces f_i in terms of the absolute atomic coordinates z_i. In other words, we have to set the absolute reference positions $\bar{z}^{1,2}_{\mathrm{CM}}$ at a given time step, given ξ_0 and $\xi(\mathbf{r})$. The $\bar{z}^{1,2}_{\mathrm{CM}}$ are determined by attributing a half of $(\xi(\mathbf{r}) - \xi_0)$ to each unit. From these $\bar{z}^{1,2}_{\mathrm{CM}}$, all the $\bar{z}_i$ are given by Eq. 7, and the forces on individual atoms can be computed. In the end, we have

$$u(\mathbf{r}, \xi_0) = \sum_{i=1}^{N} u_i(z_i, \xi_0), \tag{12}$$

$$W(t) = \sum_{i=1}^{N} W_i(t), \tag{13}$$

with $W_i(t)$ the accumulated work performed by the individual restraint $u_i(z_i, t)$, defined similarly to Eq. 3. Upon conformational changes, the internal potential energy $u_{int}(\mathbf{r}, \xi_0)$ is accumulated in the individual restraint energy terms of each unit. The individual restraints have been constructed in such a way that

$$u_{int}(\mathbf{r}, \xi_0) = u(\mathbf{r}, \xi_0) - u_{CM}(\xi(\mathbf{r}), \xi_0). \tag{14}$$

Obtaining a PMF from steered dynamics with the Jarzynski method

Considering a reaction from state A to state B, we are interested not only in the free energy difference between those two states, but also in the free energy profile of the transition. In the canonical ensemble, the potential of mean force (PMF) $\Delta G(\Xi)$ is the Helmholtz free energy profile corresponding to the integrated state density $\langle\rho(\Xi)\rangle$ along the reaction coordinate Ξ (51),

$$\langle\rho(\Xi)\rangle = e^{-\beta\Delta G(\Xi)} = \int d\mathbf{r}d\mathbf{p}\,\delta[\xi(\mathbf{r}) - \Xi]e^{-\beta H_0(\mathbf{r},\mathbf{p})}. \tag{15}$$

Note that the definition of $\langle\rho(\Xi)\rangle$ is formally correct up to a normalizing multiplicative constant of dimension length, which is usually omitted. The PMF of interest, Eq. 15, is a property of the intrinsic system. On the other hand, applying the JI, Eq. 4, directly to SMD provides the free energy change $G^C(\Xi) - G_0^C$ of the composite system,

$$e^{-\beta(G^C(\Xi) - G_0^C)} = \langle e^{-\beta W(t)}\rangle_0. \tag{16}$$

Here, $W(t)$ is the work done on the composite system, as defined in Eq. 3. The average $\langle\cdot\rangle_0$ is taken over the ensemble of trajectories with initial states ($\mathbf{r}_0$, $\mathbf{p}_0$) sampled from the canonical ensemble corresponding to the composite Hamiltonian $H_{\xi_A}(\mathbf{r}, \mathbf{p})$. To obtain the PMF for the intrinsic system, we have to find efficient ways to perform three operations:

1. Reduce from the composite to the intrinsic system (unbias).
2. Average over all $\xi(\mathbf{r})$ visited during the evolution of a given trajectory to find ΔG as a function of Ξ.
3. Estimate the exponential average $\langle e^{-\beta W}\rangle_0$ over all trajectories.

Hummer and Szabo (23) showed that

$$e^{-\beta(G(\Xi) - G_0^C)} = \langle\delta[\xi(\mathbf{r}) - \Xi]e^{-\beta(W(t) - u(\mathbf{r},\xi_0))}\rangle_0. \tag{17}$$

This corresponds to points 1 and 2 above. The weighted histogram averaging method (WHAM) (52,53) is an efficient way to estimate the average Eq. 17 from SMD time series (23,54,55). However, the direct use of Eq. 17 is problematic when the free energy barrier is high. Indeed, the exponential average $\langle e^{-\beta W}\rangle_0$ is dominated by small work values that correspond to rare events (56). Let $P(W)$ be the probability distribution of the work, which can typically be approximated by a Gaussian with a standard deviation σ. Then $P(W)e^{-\beta W}$ has a normal distribution of same width, but with its peak shifted by $\beta\sigma^2$ toward smaller values of W (24). Most work values are sampled around the peak of $P(W)$. If σ is large, the region around the peak of $P(W)e^{-\beta W}$ is not properly sampled, which results in a bias in the estimation of the exponential average. In practice, the estimator Eq. 17 can be used only when the work fluctuation σ is not much larger than k_BT. Several methods have been proposed to overcome this problem, such as the cumulant expansion method (24,30,57), block averaging (58), weighted sampling of the work values (59), or a combination of the JI with transition path sampling (60).

In this study we introduce a hybrid averaging scheme. We first perform operations 1 and 2 on separate trajectories, using a modified WHAM that takes the internal bias potential energy, Eq. 14, into account. This gives for each trajectory a corrected work profile $\overline{W}_i(\Xi)$ corresponding to the intrinsic system. In a second step, the average $\langle e^{-\beta\overline{W}(\Xi)}\rangle_0$ is estimated using the cumulant expansion method, which provides an unbiased statistical estimate of the exponential average. In the two next paragraphs, we give a detailed description of the modified WHAM and the cumulant expansion methods.

A modified weighted histogram method for individual pulling

An MD simulation with the extended Hamiltonian $H_0(\mathbf{r}, \mathbf{p}) + u(\mathbf{r}, \xi_0)$ provides, at position Ξ on the reaction coordinate, a state distribution function $\rho_{\xi_0}^{biased}(\Xi)$ which is biased. The corresponding unbiased distribution function $\rho_{\xi_0}(\Xi)$ for the intrinsic system can be obtained (operations 1 and 2 above) by applying the transformation (51)

$$\rho_{\xi_0}(\Xi) = \int d\mathbf{r}d\mathbf{p}\,\delta[\xi(\mathbf{r}) - \Xi]e^{+\beta u(\mathbf{r},\xi_0)} \times \rho_{\xi_0}^{biased}(\Xi)e^{+\beta G_{\xi_0}}e^{-\beta H(\mathbf{r},\mathbf{p},\xi_0)}.$$

Here, the undetermined constant G_{ξ_0}, defined by

$$e^{-\beta G_{\xi_0}} = \langle e^{-\beta u(\mathbf{r},\xi_0)}\rangle, \tag{18}$$

represents the free energy associated with the introduction of the biasing potential function. Decomposing the steering potential energy function according to Eq. 14 and taking terms independent of $\mathbf{r}$ and $\mathbf{p}$ out of the integral yields

$$\rho_{\xi_0}(\Xi) = e^{+\beta u_{CM}(\Xi,\xi_0)}\rho_{\xi_0}^{biased}(\Xi)e^{+\beta G_{\xi_0}} \times \int d\mathbf{r}d\mathbf{p}\,\delta[\xi(\mathbf{r}) - \Xi]e^{+\beta u_{int}(\mathbf{r},\xi_0)}e^{-\beta H(\mathbf{r},\mathbf{p},\xi_0)}. \tag{19}$$

Assuming that, in one given trajectory, important internal conformational changes happen on relatively long timescales, and that the fluctuations of $u_{int}(\mathbf{r}, \xi_0)$ are fast with respect to the CM motion, the internal potential energy function $u_{int}(\mathbf{r}, \xi_0)$, which depends on all atomic coordinates $\mathbf{r}$, can be replaced by an averaged form $\bar{u}_{int}(\Xi, \xi_0)$, which is a function of the reaction coordinate only. Technically, $\bar{u}_{int}(\Xi, \xi_0)$ is defined such that

$$e^{+\beta\bar{u}_{int}(\Xi,\xi_0)} = \int d\mathbf{r}d\mathbf{p}\,\delta[\xi(\mathbf{r}) - \Xi]e^{+\beta u_{int}(\mathbf{r},\xi_0)}e^{-\beta H(\mathbf{r},\mathbf{p},\xi_0)}. \tag{20}$$

In practice, the value of $\bar{u}_{int}(\Xi, \xi_0)$ is empirically determined as the average of $u_{int}(\mathbf{r}, \xi_0)$ in a bin of $\xi(\mathbf{r})$ centered at Ξ. Using this, the unbiased distribution function can be written as

$$\rho_{\xi_0}(\Xi) = e^{+\beta u_{CM}(\Xi,\xi_0)}e^{+\beta\bar{u}_{int}(\Xi,\xi_0)}\rho_{\xi_0}^{biased}(\Xi)e^{+\beta G_{\xi_0}}. \tag{21}$$

In WHAM (52), the total PMF at Ξ is determined as the sum of all unbiased PMFs obtained with different reference points ξ_0, weighted according to the distance between Ξ and ξ_0 (61), and the number n_{ξ_0} of sample points in window ξ_0,

$$\langle\rho(\Xi)\rangle = \sum_{\xi_0}\rho_{\xi_0}(\Xi)\frac{n_{\xi_0}e^{-\beta\left(u_w(\Xi,\xi_0) - G_{\xi_0}\right)}}{\sum_{\xi_0'}n_{\xi_0'}e^{-\beta\left(u_w(\Xi,\xi_0') - G_{\xi_0'}\right)}}. \tag{22}$$

The weight in this average is a Boltzmann term corresponding to an energy function $u_w(\Xi, \xi_0)$, which in usual WHAM is harmonic, with the same

harmonic constant as the biasing function, Eq. 2. In the case of individual restraints, at least two choices arise for u_w. The most immediate is $u_w = u_{CM} + \tilde{u}_{int}$, which means that the weighting is done with the same function as the steering. The other choice is to take only the CM distance part for the weighting, $u_w = u_{CM}$, which omits the noisy internal potential energy. In practice, this second choice turns out not to converge properly, so we focus on the first. Combining Eqs. 21 and 22 yields

$$\langle \rho(\Xi) \rangle = \frac{\sum_{\xi_0} n_{\xi_0} \rho_{\xi_0}^{\text{biased}}(\Xi)}{\sum_{\xi_0} n_{\xi_0} e^{-\beta(u_{CM}(\Xi,\xi_0) + \tilde{u}_{int}(\Xi,\xi_0) - G_{\xi_0})}}, \quad (23)$$

$$e^{-\beta G_{\xi_0}} = \int d\Xi e^{-\beta(u_{CM}(\Xi,\xi_0) + \tilde{u}_{int}(\Xi,\xi_0))} \langle \rho(\Xi) \rangle. \quad (24)$$

This constitutes the specific WHAM system of equations for individual restraints with fixed reference points ξ_0. In this case, an initial guess for G_{ξ_0} is provided by estimating offsets which make the PMFs of neighboring ξ_0 overlap approximately, and Eqs. 23 and 24 are solved iteratively. This method could be used for umbrella sampling (62) with individual restraints.

In the case of SMD, the picture is slightly different, since ξ_0 sweeps the whole range of the reaction coordinate during one trajectory, instead of being fixed. Accordingly, $\xi(\mathbf{r})$ coming from a single trajectory is also distributed over the whole range. Histograms are collected in bins located at fixed Ξ, and data coming from different trajectories are summed up indifferently. According to the JI, we define

$$\rho_{\xi_0}^{\text{biased}}(\Xi) = \frac{\langle \delta[\xi(\mathbf{r}) - \Xi] e^{-\beta W(\xi_0)} \rangle_0}{\langle e^{-\beta W(\xi_0)} \rangle_0}, \quad (25)$$

and the initial guess for the offset of window ξ_0 is $e^{-\beta G_{\xi_0}} = \langle e^{-\beta W(\xi_0)} \rangle_0$. In addition, the number of points n_{ξ_0} in a window is considered approximately constant, and is taken out of the weighting term. Inserting these modifications in Eq. 23 yields an expression similar to the adapted WHAM of Hummer and Szabo (23,55) with the addition of the $\tilde{u}_{int}(\Xi, \xi_0)$ term. This expression can be used directly to find $\Delta G(\Xi)$ from simulations in which the dissipative part of the steering work is small and the direct estimation of the exponential average is possible.

In the present case, we leave the intertrajectory averaging (i.e., operation 3) for the next step, namely the cumulant expansion method (see below). We nonetheless use the modified WHAM on each trajectory i separately to find unbiased and smoothed work profiles $\overline{W}_i(\Xi)$ (i.e., operations 1 and 2). The corresponding WHAM equations are

$$\overline{W}_i(\Xi) = -\frac{1}{\beta} \ln \frac{\sum_{\xi_0} \langle \delta[\xi(\mathbf{r}) - \Xi] e^{-\beta W_i(\xi_0)} \rangle_0 e^{+\beta G_{\xi_0}}}{\sum_{\xi_0} e^{-\beta \left(u_{CM}(\Xi,\xi_0) + \tilde{u}_{int}(\Xi,\xi_0) \right)} e^{+\beta G_{\xi_0}}} \quad (26)$$

$$e^{-\beta G_{\xi_0}} = \int d\Xi e^{-\beta \left(u_{CM}(\Xi,\xi_0) + \tilde{u}_{int}(\Xi,\xi_0) \right)} e^{-\beta \overline{W}_i(\Xi)} \quad (27)$$

The evaluation of the numerator in the above equation consists in building a histogram of $e^{-\beta W_i(\xi_0)}$ with bins of width Δ_Ξ centered at positions Ξ. In the single trajectory case, the initial guess $e^{-\beta G_{\xi_0}} = e^{-\beta W(\xi_0)}$ allows a simplification in the numerator for the first iteration of the WHAM method,

$$\overline{W}_i(\Xi) = -\frac{1}{\beta} \ln \frac{\sum_{\xi_0} \Theta_\Xi[\xi(\mathbf{r})]}{\sum_{\xi_0} e^{-\beta \left(u_{CM}(\Xi,\xi_0) + \tilde{u}_{int}(\Xi,\xi_0) \right)} e^{+\beta W_i(\xi_0)}}. \quad (28)$$

The indicator function Θ_Ξ is one if $\xi(\mathbf{r})$ is in the interval $[\xi - \Delta_\Xi, \xi + \Delta_\Xi]$, and zero otherwise.

The cumulant expansion method

To bypass the direct estimation of an intertrajectory exponential average (operation 3), the cumulant expansion method is often used (24,30,45,63). The idea is to expand the logarithm of the exponential average in terms of cumulants,

$$\Delta G(\Xi) = -\frac{1}{\beta} \ln \langle e^{-\beta \overline{W}(\Xi)} \rangle_0 = \sum_{i=1}^{\infty} C_i \frac{(-\beta)^i}{i!}. \quad (29)$$

The first cumulant is $C_1 = \langle \overline{W} \rangle$, where $\langle \cdot \rangle$ is the arithmetic average of the smoothed and unbiased work values obtained from the various trajectories at a given reaction coordinate Ξ. The second cumulant is $C_2 = \sigma^2_{\overline{W}}$, the sample variance of the obtained work values. Thus, the second-order expansion reads

$$\Delta G(\Xi) = \langle \overline{W}(\Xi) \rangle - \frac{\beta}{2} \sigma^2_{\overline{W}}(\Xi). \quad (30)$$

Marcinkiewicz's theorem (64) states that if and only if the work distribution is Gaussian, all but the first two cumulants in the expansion vanish. In all other cases, there are an infinite number of nonvanishing cumulants. This property is of relevance here, because higher moments are difficult to estimate from limited samples. The second-order expansion provides an accurate estimation if the work distribution is close to Gaussian, which is supported by a couple of arguments. First, in near-equilibrium regimes the work distribution approaches a Gaussian. In this perspective (57), the JI reduces to predating near-equilibrium results (65) similar to Eq. 30, which are valid in the linear response regime, and are related to the fluctuation-dissipation theorem. Second, the Gaussian character of the work distribution, even far from equilibrium, is favored by the choice of a stiff steering function (24).

Assume that we have n work values drawn from a Gaussian distribution. Both estimators of $\langle \overline{W} \rangle$ and $\sigma^2_{\overline{W}}$ (when normalized with $n-1$) are statistically unbiased. The expected statistical error on ΔG can be estimated, assuming that the statistical errors on the mean and variance are uncorrelated (63):

$$\text{var}(\Delta G(\Xi)) = \frac{\sigma^2_{\overline{W}}}{n} + \frac{\beta^2}{2} \frac{\sigma^4_{\overline{W}}}{(n-1)}. \quad (31)$$

When using the truncated cumulant expansion, Eq. 30, two kinds of error are involved: the error due to neglecting higher order terms, and the error due to the estimation of each terms with finite sampling. Calculating the exponential average in Eq. 17 directly yields no truncation error, but the sampling error can become prohibitive when $\sigma^2_{\overline{W}}$ is large. On the contrary, $\langle \overline{W} \rangle$ and $\sigma^2_{\overline{W}}$ are easier to estimate from a finite data set because they are unbiased statistical estimators, but higher-order terms of the cumulant expansion are truncated.

Simulation setup

The wild-type A6/Tax/HLA-A0201 x-ray structure (11) was taken from the 1ao7 entry of the Protein Data Bank, and the P6A mutant structure (12) from the 1qrn entry. To reduce the system size, only the V_α and V_β domains of the TCR are included in the simulation. This is justified by experimental evidence (66) that the V_α and V_β domains alone (expressed as a single chain sFv) keep the same structure and MHC reactivity as the full TCR molecule. The resulting model includes a total of 605 residues. The proteins are modeled with the GROMOS 43A1 force field (67) and solvated in constrained (68) SPC water (69). Explicit water molecules are necessary for an accurate description of buried surface solvation upon unbinding, including water bridges and entropic effects due to the liberation of trapped water molecules. Indeed, a number of bound water molecules have been resolved at the TCR-pMHC interface (11,12). In addition, a detailed MD study evidenced (70) the important role of some water molecules at the TCR-pMHC interface. All water molecules resolved in the crystal structures are kept in their original initial position as the protein is inserted in preequilibrated water. Nine Na^+ counterions are added to balance the net charge of the system. The simulation box is chosen such that the CMs of the MHC and the TCR are aligned along the z axis. A weak restraint of 100 kJ mol^{-1}nm^{-2} in the (x, y) plane is applied to

the CMs of the MHC and the TCR to keep them aligned along the z axis. This auxiliary restraint is perpendicular to the reaction coordinate and thus never accumulates work and does not interfere with the free energy measurement. The protein is surrounded by at least 1.2 nm of water on each of the x and y sides of the box. An additional 1.6 nm is left in the z direction, to allow space for the dissociation. This results in 25,990 water molecules in a $7.6 \times 8.1 \times 14.4$ nm box. Long-range electrostatic interactions are treated with particle mesh Ewald summation (71). A twin-range cutoff scheme is used for the Lennard-Jones (LJ) interactions in which interactions are calculated every step up to a cutoff distance of 0.8 nm and every five steps up to 1.4 nm. All covalent bonds involving hydrogens are constrained at their ideal lengths using SETTLE (72), a version of the SHAKE (73) algorithm. Proteins and solvent are coupled to two separate Nosé-Hoover (74) thermostats with time constant 0.1 ps. The pressure is controlled by a Parrinello-Rahman (75,76) barostat, with time constant 0.5 ps. This combination of thermostat and barostat should preserve the correct NPT ensemble.

The system is prepared as follows. Random velocities are first assigned according to a Maxwell distribution at 100 K. Then the system is heated up to 300 K in 100 ps at constant volume, and with atoms of the backbone and side chains up to the C_β carbon restrained to the crystal positions with harmonic potentials of 1000 kJ mol^{-1} nm^{-2}. A stable RMSD of ~0.20 nm on backbone atoms is observed with respect to the crystal structure after 800 ps of equilibration.

A standard Jarzynski simulation requires a long preliminary reference simulation at equilibrium in the initial state. Decorrelated configurations with velocities are then chosen from this equilibrium trajectory as starting points for the pulling runs. We call this protocol S for sequential. When a computer grid is used, calculating the reference trajectory is very inefficient. Instead, the following protocol R (for random) can be used. Different replicas are started on independent processors before the heating-up phase described above, by assigning different initial random velocities to each of them. After a temperature of 300 K is reached, 700 ps of equilibration are performed on each replica. Protocol R has two advantages over the standard protocol S, besides the practical aspect related to grid computing. First, the structure at the end of each short equilibration cannot have deviated much from the crystal structure, as could happen after one extremely long trajectory, due to MD inaccuracies. Second, the diversity of structures obtained at the end of the independent equilibrations is much bigger than the diversity of a sample of consecutive frames of one long equilibration (77). This is likely to provide a better convergence of the average in Eq. 4.

In protocol R, the last 200 ps of each equilibration run are used to compute the average CM distance ξ_A, as well as the average internal coordinates $\{\overline{\zeta_i}\}_{i=1}^{N}$. This average structural information is specific to each trajectory, and is used as initial distance and reference structure for the individual restraints, Eq. 8. Next, the individual restraints are applied on the atoms specified above with a resulting harmonic constant of $k_{CM} = 2 \times 10^4$ kJ mol^{-1}nm^{-2}. This k_{CM} is chosen stiff enough to have a good spatial resolution in the free energy profile and to keep the work distribution Gaussian (24), while not damping the thermal behavior of the system. The corresponding harmonic constant k_i, Eq. 11, on one carbon atom is 69 kJ mol^{-1} nm^{-2}, which allows for a typical displacement of 0.27 nm at k_BT. This shows that in addition to being totally free in the (x, y) plane, local parts of the protein backbone are allowed to relax in the z direction as well, despite the structural restraints. The composite system is then further equilibrated during 300 ps with ξ_0 fixed at ξ_A. Finally, the pulling itself is started. A pulling speed of $v = 5 \times 10^{-4}$ nm/ps is chosen as a tradeoff between staying as close to equilibrium as possible and keeping the computing time within manageable limits. With these settings, 2 nm are covered in 4 ns of simulation. One steering trajectory including equilibration as described above requires ~6 weeks of calculation on a 1.3 GHz Itanium2 processor. The simulation protocol for the P6A mutant is exactly the same.

The two main data sets exploited in this study are composed of 152 trajectories of the TCR-Tax-MHC complex, and 162 trajectories of the P6A complex. These trajectories were generated with the R protocol described above using the GROMACS 3.3.1 MD package (78–80), modified for individual atom pulling. The precise number of trajectories generated depended on the computer resources at hand. Additional data sets from preliminary or subsequent control simulations of the TCR-Tax-MHC complex are used as well to assess the free energy results. These additional data sets differ by the GROMACS (gmx) version, the protocol (S of R, see above), and the number of trajectories. We designate these conditions with a condensed notation such that the aforementioned main data set for Tax corresponds to (*gmx 3.3.1 - R - 152 traj*). The other sets are (*gmx 3.1.4 - S - 68 traj*), (*gmx 3.1.4 - S - 133 traj*), and (*gmx 3.3.1 - S - 129 traj*). Note that simulations with the older GROMACS 3.1.4 are considered less reliable, in particular because of an inaccurate implementation of the temperature and pressure feedback in the context of the leap-frog integration scheme (see (81)). This issue was corrected in gmx 3.3.1.

RESULTS AND DISCUSSION

Steered molecular dynamics

Fig. 3 shows the evolution of the steering potential energy along the reaction coordinate. Two contributions are shown. First, $u_{CM}(\xi(\mathbf{r}), \xi_0)$ directly reflects the resistance of the system to the dissociation force. It increases sharply to a maximum at ~0.2 nm distance at which most contacts have to be broken. Then $u_{CM}(\xi(\mathbf{r}), \xi_0)$ decreases again, to reach zero approximately at a distance of 1.0 nm, at which all interactions have faded (see Fig. 5). The Tax peptide induces a higher steering potential energy than the P6A mutant, indicating that the TCR dissociation energy barrier is higher (with this steering velocity). The second contribution to the steering potential energy is $u_{int}(\mathbf{r}, \xi_0)$, which is related to the internal rearrangement of each part. We first observe a sharp increase due to the fact that atoms far from the TCR-pMHC interface are free to follow the steering restraint and atoms close to the interface are held back. This increase may also be caused by a propensity of the TCR and the pMHC to rotate with respect to each other (see Fig. 2 *b*), which is prevented by the individual restraints. Beyond 1.0 nm, $u_{int}(\mathbf{r}, \xi_0)$ continues to increase, due to slow internal rearrangement. Because no strong external force acts on the proteins at this point in the process, this shows that the system is able to rearrange by itself despite the individual restraints.

The work profiles obtained with protocol R for 152 pulling trajectories of the TCR-Tax-MHC complex are shown in Fig. 4. For each trajectory i independently, profiles of $\overline{W}_i$ have been obtained by smoothing and unbiasing the raw work data with the iterative modified WHAM, Eq. 26. We notice that, in this case, subsequent WHAM iterations change only marginally the profile given by the initial guess, Eq. 28 (data not shown). In the first 0.4 nm of displacement, the resulting work curves undergo a steep increase, as most hydrogen bonds and van der Waals contacts are broken. At $\xi = 1$ nm and further, when all interactions have vanished, a plateau value is reached. The average skewness (describing the asymmetry of the distribution), and kurtosis (describing the weight of the tails) observed between $\xi = 1$ nm and $\xi = 2$ nm are -0.026 and 3.023, respectively (0 and 3 correspond to a Gaussian distribution). At all distances, the work distribution

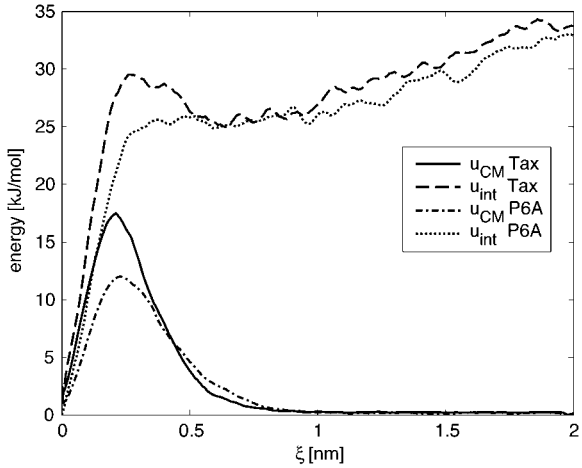

FIGURE 3 Contributions to the steering potential energy $u(\mathbf{r}, \xi)$ along the reaction coordinate ξ, for the Tax and the P6A complexes. The two upper lines show the part $u_{\mathrm{CM}}(\xi(\mathbf{r}), \xi)$ from Eq. 10, which depends on the CM distance. The two lower lines show $u_{\mathrm{int}}(\mathbf{r}, \xi)$ from Eq. 14, which corresponds to internal rearrangements in the TCR and pMHC.

is consistent with a Gaussian distribution according to a 5% Kolmogorov-Smirnov test (data not shown). Indeed, the Gaussian character of the work distribution even far from equilibrium is favored by the choice of a stiff steering potential energy function (24).

We investigated whether the final work necessary to dedock the complex in each trajectory could be correlated to some spatial or energetic observable of the system at the beginning or at the end of the process. A spatial analysis of the dedocking pathways of the TCR with respect to the pMHC was carried out (not shown). No spatial grouping of trajectories with low work values could be identified, which would constitute a funnel along which the TCR would preferably dedock. Furthermore, no correlation appears between the final work and either of the initial or final x, y, or z relative CM positions of the TCR and pMHC, or their relative orientation in the (x, y) plane.

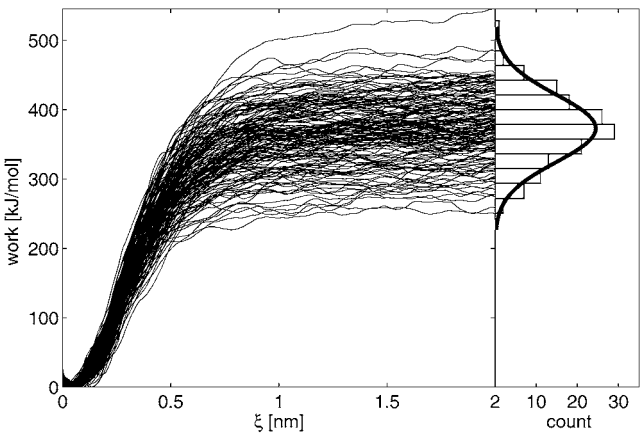

FIGURE 4 Collection of 152 work profiles along the reaction coordinate, smoothed and unbiased using Eq. 26. The right panel shows an histogram of this distribution (taken at $\xi = 1.7$ nm), with the fitted Gaussian distribution used in the cumulant expansion method.

Fig. 5 *a* shows the LJ interaction energy between the TCR and the pMHC, as a function of the reaction coordinate. The protein coordinates were extracted from configurations taken at 200 ps time intervals from each steered trajectory, which corresponds to 0.1 nm intervals of ξ_0. For each of these configurations, the LJ interaction energy between TCR and pMHC was calculated, including the separate contributions of the Tax peptide and the MHC itself. For all configurations at a given time point, these LJ energies were then averaged over all trajectories. We see that beyond 1.0 nm CM distance all van der Waals contacts are broken. The inset shows the correlation that exists between the LJ energy integrated along the trajectories and the final work. This indicates that the van der Waals and steric interactions play a determining role in the dedocking mechanism. The P6A complex has a similar

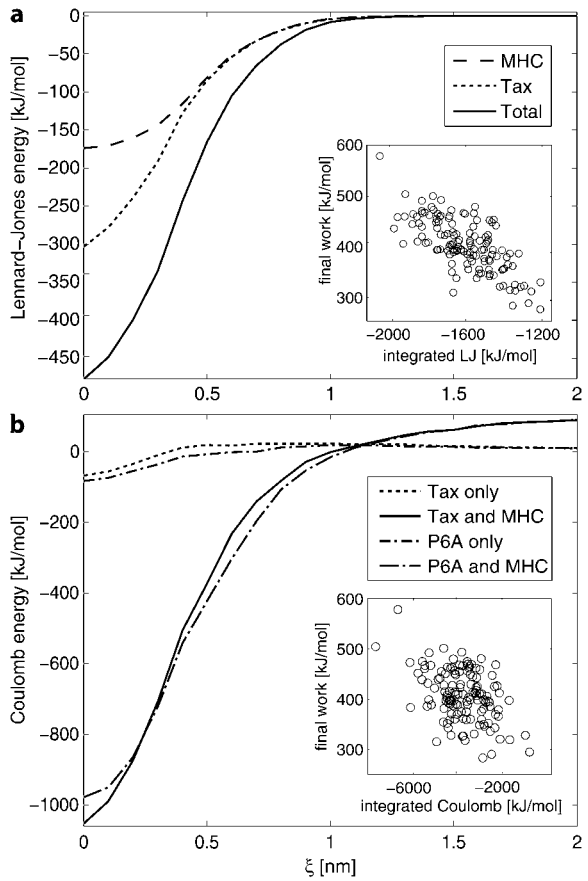

FIGURE 5 (*a*) The van der Waals interaction energy (excluding water) as a function of the reaction coordinate, averaged over 152 unbinding trajectories with the Tax complex. The inset shows, for each trajectory, the final work as a function of the integrated van der Waals energy. (*b*) Electrostatic interaction energies (excluding water and with a relative permittivity of 1) averaged over 152 trajectories for the Tax complex and 162 trajectories for the P6A complex. The inset shows the correlation between final work and integrated electrostatic energy.

behavior. The data for P6A is not shown on Fig. 5 *a* because the curves are almost indistinguishable from those of Tax. The total LJ interaction energy in the bound P6A complex is just 11 kJ mol^{-1} less favorable than in the Tax complex. Note that, as apparent in Fig. 6, no definitive conclusion on the role of the van der Waals contacts in the dissociation process can be drawn without considering the resolvation and internal reorganization energy changes.

The Coulomb interaction energy between the TCR and the pMHC was obtained as follows. For each configurations, the solvent was stripped away and the Coulomb interaction energy was calculated without cutoff in a nonperiodic setup. A relative permittivity of 1.0 was used, which is accurate at short distances, but neglects the dielectric effect of water at larger distances. However, given the fact that an SPC water molecule is itself not polarizable, one expects charge shielding effects to appear only at distances allowing several water molecules to reorient. Fig. 5 *b* shows the electrostatic interaction energy along the reaction coordinate for both Tax and P6A complexes, which display a very similar behavior. At distances larger than 1.7 nm, a plateau is reached, where the interaction is slightly repulsive, probably due to the fact that the MHC has a total charge of -8 *e* and the TCR of -1 *e*. This long-distance contribution can easily be shielded by ions and the solvent. The strong attraction at short distance is explained by complementary surface charges and dipoles, as well as hydrogen bonds. It appears that the contribution of the peptide to the total binding electrostatic energy is very small compared to the contribution of the MHC, which contrasts with the repartition of the LJ interaction energy.

In Fig. 5 *b*, the bound P6A complex seems to be less stabilized by electrostatic interactions than the bound Tax complex. Indeed, at $\xi = 0$, the average Coulomb interaction energy is -977 ± 28 kJ mol^{-1} for the P6A complex, compared to -1052 ± 34 kJ mol^{-1} for the Tax complex. The confidence intervals given represent two standard deviations of the values collected in the trajectory sets. Unexpectedly, it appears in Fig. 5 *b* that the discrepancy is entirely due to the MHC-TCR contribution, rather than to the peptide itself, which even contributes slightly in the opposite way. To assess the significance of the observed difference in interaction electrostatic energy, we calculated this quantity on the last 200 ps of equilibration of the bound complexes (*R* protocol, without steering potential). We get on average -987 ± 28 kJ mol^{-1} for P6A and -1052 ± 29 kJ mol^{-1} for Tax. This confirms a difference in interaction energy of $\sim$70 kJ mol^{-1}. This difference might be due to subtle differences in the TCR-pMHC structures despite their remarkable overall similarity as judged by x-ray crystallography (12). Ultimately, this difference in interaction electrostatic energy may contribute toward the difference in association free energies of the Tax and P6A complexes. For individual unbinding trajectories, however, the inset in Fig. 5 *b* shows that there is little correlation between the electrostatic energy integrated along the trajectory and the final work. Interestingly, it has been noted before (82) that the protein-ligand LJ interaction energy correlates better with the affinity than the electrostatic interaction energy, which is well compensated upon solvation by polar interactions with water molecules.

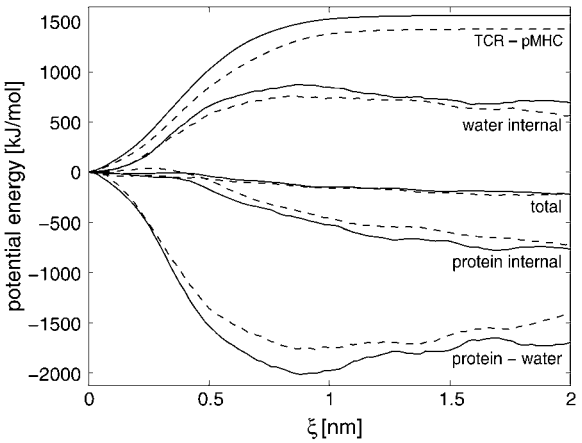

FIGURE 6 Evolution of the potential and interaction energies in and between different parts of the system upon dissociation. Solid lines represent the Tax complex and dashed lines represent the P6A complex. (Here, the term *protein internal* designates the sum of the internal potential energy in the TCR and in the pMHC. *TCR-pMHC* designates the interaction energy between the two parts. Note that the categories *TCR-pMHC*, *water internal*, *protein internal*, and *protein-water* are mutually exclusive, and their contributions sum up to the total potential energy.)

In addition to looking at van der Waals and electrostatic interaction energies between the TCR and the pMHC, the present approach allows us to gather sufficient statistics to compute the potential energy changes in (and between) different parts of the system, including the solvent. In the following, we call potential energy the sum of the LJ, electrostatic and bonded terms of the force field. Note that the kinetic energy is kept on average constant in the protein and in the solvent by the two thermostats. Fig. 6 thus provides a complete energetic balance of the dissociation process, including the protein and solvent internal energies, as well as the TCR-pMHC and protein-solvent interaction energies. To calculate separately the solvent contribution to the electrostatic energy in the periodic system, a cutoff scheme had to be used. Therefore all electrostatic energies in Fig. 6 are calculated with a cutoff of 1.4 nm and a reaction field correction (83). At each time point, energies were averaged over all available trajectories, after which residual statistical noise was smoothed out using running window averaging. Note that the average absolute value of the potential energy is -1.16×10^6 kJ mol^{-1} for the Tax complex, composed mainly of the Coulomb part (-1.34×10^6 kJ mol^{-1}) and the LJ part ($+1.57 \times 10^5$ kJ mol^{-1}). The root mean-square fluctuation of the potential energy in a single trajectory is 1.13×10^3 kJ mol^{-1} (1.88×10^3 and 1.17×10^3 kJ mol^{-1} for Coulomb and LJ energies, respectively). This means that $\sim$99% of the fluctuations on the potential energy are within $+3300$ and -3300 kJ mol^{-1} around the mean value, and are

thus much larger than the variations observed on Fig. 6. This underlines the fact that statistics over many trajectories are necessary to be able to extract a meaningful average behavior of the system.

The TCR-pMHC interaction energy shown in Fig. 6 is the sum of the LJ and Coulomb contributions shown in Fig. 5 (except for the fact that the electrostatic interaction energy is slightly less accurate here due to the use of a cutoff). We see that this interaction energy change is largely compensated by the contributions of the solvent. Upon dissociation, the solvation of residues buried at the interface in the bound state causes a large decrease of the protein-water interaction energy. Concomitantly, the internal energy of the solvent increases as the arrangement of water molecules is more constrained close to the newly exposed protein surface than in the bulk. Overall, the contributions of the solvent are large, both in interaction with the protein or internally, which justifies a posteriori using explicit water molecules for this study. The internal energy of the proteins decreases upon dissociation, showing that each part of the complex relaxes slightly to a more favorable conformation as the TCR-pMHC contact is released. This trend is consistent with the steady increase of the internal part of the steering potential observed in Fig. 3. In the case of the P6A complex, the behavior of all contributions mentioned above is the same as for the Tax complex, but of lesser magnitude: to a smaller interaction energy change corresponds a smaller solvation energy change.

The variation of the total potential energy is very small compared to each of the contributions, and appears to be a tradeoff between TCR-pMHC interaction energy and solvation effects. Interestingly, the total potential energy change of the Tax and P6A complexes cannot be differentiated, both displaying a 220 kJ mol^{-1} decrease. This decrease could have two explanations. First it could reflect a genuine enthalpy change upon dissociation of the system. However, we have to remain very cautious about this figure, since it could also result from an insufficient equilibration of the system before the pulling is initiated (despite the 1-ns total equilibration time for each trajectory). In this second case, a part or the whole of the 220 kJ mol^{-1} variation should not be attributed to the TCR-pMHC dissociation mechanism, but rather to the fact that the system might not have relaxed completely to equilibrium before the pulling. We have to keep in mind that this trend is extremely small with respect to the absolute value of the total energy and its large fluctuations. Such an energy change would remain unnoticed if only a single trajectory was studied. To the best of our knowledge, no accurate MD simulation convergence study has been reported on large sets of nanosecond-long trajectories.

Binding free energy profile estimations

The JI, Eq. 4, together with the modified WHAM method, Eq. 26, for individual pulling were applied to the two main data sets composed of 152 trajectories for the Tax complex and 162 trajectories for the P6A complex, as described in Methods. The resulting PMFs are shown in Fig. 7. These PMFs indicate dissociation free energy differences of -110 and -210 kJ mol^{-1} for the Tax and P6A complex, respectively.

However, these numbers cannot rigorously be compared to the experimental dissociation free energies mentioned in the Introduction. Indeed, the final unbound state in our SMD simulations does not correspond to the standard state, for which experimental free energies are given (solution at standard concentration, 1 mol/L). Instead, the system is still restrained by the steering potential, which prevents each of the TCRs and pMHCs from freely rotating and occupying the standard volume $V_0 = 1660$ Å^3. Therefore, the corresponding rotational and translational entropy must be taken into account separately to obtain absolute binding free energies from the PMFs. The entropic cost of restraining a system can be evaluated, based on a quasiharmonic approximation for angular and positional fluctuations in the restrained state. Such expressions have been derived in relation to the MM/PBSA method (84,85), the double decoupling method (86), and a PMF-based method (87).

Here, we describe the relative position of the TCR with respect to the pMHC using the Cartesian separation (x, y, z) of their centers of mass. Cartesian coordinates are appropriate, since z is the reaction coordinate. The relative orientation of the TCR is given by the three following angles, after superposition of the pMHC molecules: the dihedral ϕ around the z axis; the angle θ between the z axis and the vector v_{CM} connecting the CMs of the TCR V_α and V_β domains; and the dihedral ϕ around v_{CM}. We note $\{\sigma_x, \sigma_y, \sigma_z, \sigma_\phi, \sigma_\theta, \sigma_\psi\}$ the fluctuations in positional and angular coordinates observed among all pulling trajectories. Note that, following closely the derivation in Woo and Roux (87), all of the above fluctuations correspond to the final unbound conformations, except σ_z, which describes the bound complex. With θ_0 the

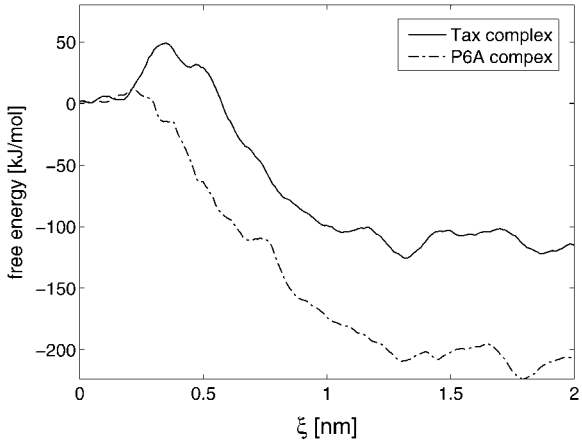

FIGURE 7 Potentials of mean force obtained from the Jarzynski method with 152 trajectories for the Tax peptide and 162 trajectories for the P6A mutant (gmx 3.3.1, *R* protocol).

average value of θ, the translational and rotational contribution to the dissociation free energy can be written

$$\Delta G^{\text{trans/rot}} = -k_{\text{B}}T\log\frac{8\pi^2 V_0}{(2\pi)^3\sin(\theta_0)\sigma_{\text{x}}\sigma_{\text{y}}\sigma_{\text{z}}\sigma_\phi\sigma_\theta\sigma_\psi}. \quad (32)$$

For the Tax complex, we get $\Delta G^{\text{trans/rot}} = -28.7$ kJ mol^{-1}, which should be added to the unbinding free energy difference from the PMF. The translational part amounts to -9.1 kJ mol^{-1}, most of which, -5.7 kJ mol^{-1}, is due to the z component. The major contributions to $\Delta G^{\text{trans/rot}}$, however, come from the θ and ψ components, which account for -8.4 and -8.2 kJ mol^{-1}, respectively, denoting the strong propensity of the individual restraints to maintain the orientation of the TCR along the z axis. For the P6A complex, results are similar, with $\Delta G^{\text{trans/rot}} = -27.9$ kJ mol^{-1}.

Adding $\Delta G^{\text{trans/rot}}$ to the dissociation free energies from the PMF give ΔG values of -139 and -238 kJ mol^{-1} for the Tax and P6A complex, respectively. These ΔG are largely underestimated as compared to the experimental results (32.2–39.2 kJ mol^{-1} for Tax and ~22.6 kJ mol^{-1} for P6A). It is difficult to predict how the progressive entropy gain due to the progressive increase in rotation and translation freedom along the dissociation reaction coordinate modifies the shape of the PMF. The dissociation free energy barrier is, however, not likely to be affected much, since the complex in the transition state is still partially bound, with most of the relative motion between the two partners restrained. Thus the PMF should provide a ΔG^{off} directly comparable to experiment. For the Tax complex, the calculated $\Delta G^{\text{off}} = 50$ kJ mol^{-1}, also underestimates the experimental dissociation free energy barrier (79.5 kJ mol^{-1}). The calculated ΔG^{off} for the P6A complex is very low, but there is no experimental counterpart.

The statistical error related to the use of the second-order cumulant expansion, Eq. 30, can be estimated with Eq. 31. This results in an expected standard deviation for $\Delta G(\Xi)$ of 17 kJ mol^{-1} at the barrier, and 55 kJ mol^{-1} in the unbound state (see also Fig. 8 *a*). Even with such large error bars, the calculated results cannot be reconciled with the experiment. Our simulations are nonetheless able to unambiguously differentiate the behavior of the P6A mutant. The calculated free energy difference between Tax and P6A has the right sign, both at the barrier and in the dissociated state, and is significant with regard to the statistical errors mentioned above. This is not trivial given the very minute and local character of the mutation, as well as the great structural similarity of both complexes (12) (see Fig. 1 *b*).

During the simulation, the shape of the lattice induced by the periodic boundary conditions changes from one big protein per cell to two separated parts. Therefore, periodicity artifacts—if any—could be different in the bound and unbound states, and may consequently affect the calculated PMF. The artifacts can be of two kinds (88,89). First the long-range electrostatic energy can be affected by the periodic lattice of charges. Second, the rearrangement of the water molecules around the protein is disturbed by the periodic images, which influences the polar part of the solvation free energy. To assess these effects in this simulation, selected

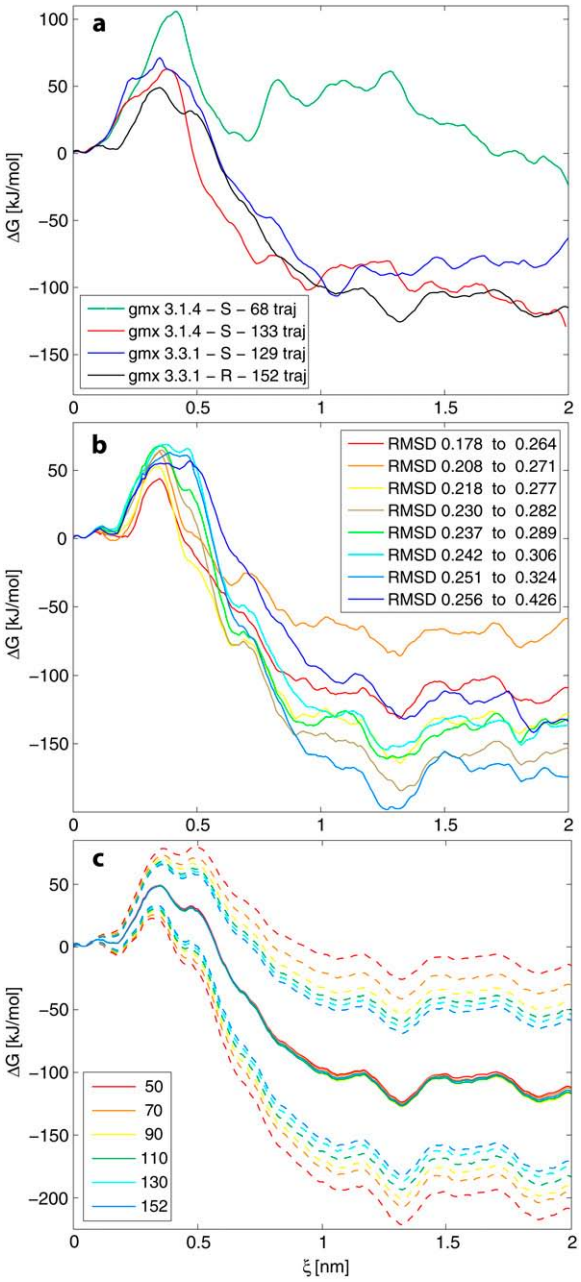

FIGURE 8 (*a*) Potentials of mean force obtained from additional data sets. The legend gives the GROMACS (79) version used, the protocol for initial conditions (*S*, sequential; *R*, random), and the number of trajectories in the data set. (*b*) Potentials of mean force obtained from sets of trajectories ranked according to the RMSD of the CDRs just before the pulling is started. The RMSD is calculated on all CDRs (except CDR2β, which has no contact with pMHC (12)), after superposition of the MHC α1 and α2 chains on the crystal structure. (*c*) Trajectory set size effects. For each size, 1000 random sets of trajectories were drawn, and the average PMF calculated with Eq. 30. The dashed lines show, for each set size, the average expected standard deviation on ΔG according to Eq. 31.

configurations were taken from each trajectory and the solvent removed. For the electrostatic part, the difference between the full Coulomb energy (without cutoff) of the isolated protein and the particle mesh Ewald energy of a periodic lattice of proteins is calculated. For the solvation part, the difference between Poisson-Boltzmann terms in the isolated and periodic configurations is calculated. We verified (data not shown) that although each individual artifact has a sizable magnitude, the two compensate, and the resulting contribution to the PMF is negligible.

As a consistency check for the method, additional PMF results obtained with data sets (*gmx 3.1.4 - S - 133 traj*) and (*gmx 3.3.1 - S - 129 traj*) of the TCR-Tax-MHC complex are shown on Fig. 8 *a*. The main observation is that using the *S* or *R* protocols with gmx 3.3 or using the *S* protocol with 133 trajectories of gmx 3.1.4 yield similar results. The observed differences between protocols do not seem to be significant in regard to the statistical error expected for the cumulant expansion method. Overall, the three lower curves on Fig. 8 *a* confirm the robustness of the calculations previously made with the main data set (Fig. 7): ΔG^{off} lies between 50 and 60 kJ mol^{-1} and the calculated ΔG is ~ -100 kJ mol^{-1}. Although these values are not consistent with experiment, the method seems to reach some level of convergence with 130–150 trajectories. If the same kind of robustness can be assumed for the P6A mutant, the 100 kJ mol^{-1} free energy variation with respect to the wild-type observed in Fig. 7 is significant.

The upper curve on Fig. 8 *a*, (*gmx 3.1.4 - S - 68 traj*), is the first result we obtained in an early stage of the study. Note that the 68 trajectories of set (*gmx 3.1.4 - S - 68 traj*) are a subset of (*gmx 3.1.4 - S - 133 traj*), whose initial conditions were subsequent configurations from the same reference trajectory. The obvious large difference with the other PMFs obtained subsequently with bigger trajectory sets could arise from two different reasons. First, if we consider that the (*gmx 3.1.4 - S - 68 traj*) PMF yields ΔG^{off} and ΔG values closer to experimental results, we might conclude that it is a better Jarzynski estimate, although based on fewer trajectories. This would make sense, for example, if the first part of the reference trajectory (*S* protocol) was closer to the crystal structure, with better conserved contacts between the pMHC and the TCR. Due to force-field inaccuracies, further points on the reference equilibrium trajectory could no longer be representative of the physical TCR-pMHC complex, and the corresponding trajectories would spoil bigger sets, such as (*gmx 3.1.4 - S - 133 traj*) or (*gmx 3.3.1 - S - 129 traj*). To check whether the RMSD of the initial conformation with respect to the crystal structure had an influence on the final PMF, we ranked trajectories according to the RMSD of the CDRs (except CDR2β, which has no contact with pMHC (12)), with the MHC α1 and α2 chains aligned on the crystal structure. We then performed the cumulant expansion on various subsets with low RMSD (0.178–0.264 nm) to high RMSD (0.256–0.426 nm). Fig. 8 *b* clearly shows that there is no direct influence of the RMSD on the PMF. This first reason is further contradicted by set (*gmx 3.3.1 - R - 152 traj*) obtained with the *R* protocol, in which the short duration of the independent equilibration runs guarantees that the various initial conditions for pulling remain close to the crystal structure.

The second and most likely reason for the discrepancy of (*gmx 3.1.4 - S - 68 traj*) would be that using only a small number of trajectories leads to nonconverged cumulant terms and an unreliable PMF. To test whether there is a systematic sample size effect on the estimation of the PMF, we drew 1000 random subsets for each size {50, 70, 90, 110, 130} from the set (*gmx 3.3.1 - R - 152 traj*). For each sample size, the results of the cumulant expansion, Eq. 30, were averaged over the 1000 subsets. The resulting average PMF are shown on Fig. 8 *c*, which shows that there is no systematic bias due to the sample size. Nonetheless, the expected statistical errors estimated from Eq. 31 and averaged over the 1000 subsets is higher for smaller samples, as shown by the dashed lines on Fig. 8 *c*. Given a single subset of 68 trajectories, the statistical error can be as high as 100 kJ mol^{-1}. Thus, the (*gmx 3.1.4 - S - 68 traj*) PMF comes as a warning that poor convergence can have a dramatic effect on Jarzynski free energy estimates.

To conclude the discussion on the PMF estimation, we can say the following. In the three largest trajectory sets of Fig. 8 *a*, the second-order cumulant expansion, Eq. 30, is converged, but to a value that strongly underestimates experimental results. Standard causes for inaccuracies in MD, such as force-field approximations, cutoffs, and numerical integration are not likely to account alone for the observed discrepancy. We see two possible explanations for this issue.

The first explanation follows from the observation that the potential energy change of -220 kJ mol^{-1} shown in Fig. 6 corresponds to an enthalpy change during the simulation. As mentioned above, it is impossible to say what proportion of this potential energy change corresponds to a genuine enthalpy change due to the transition between the bound and unbound state of the system and what part results from an incomplete equilibration of the bound state. In both cases the potential energy change should reflect on the dissociation PMF. Regarding the case of an artifactual energy drift in the system during the Jarzynski experiment, it is informative to refer to the JI derivation specific to thermostated and barostated systems published previously (40,41). If an homogeneous energy drift term $h(t)$ is added to the pseudo-Hamiltonian describing the system and the thermo-barostat, the same derivation can be carried out. Not surprisingly, we find that, if the definition of W is maintained as Eq. 3, $\langle e^{-\beta W} \rangle = e^{-\beta[\Delta G + h(\tau)]}$. This indicates that the measured free energy difference will indeed comprise the artifactual energy drift. It is, however, difficult to say to what extent a slight dynamical reorganization of a few atoms far from the TCR-pMHC interface projects, in practice, on the reaction coordinate and influences the dissociation work measured along it. On a different note, we observe that protocol *S*, in which

initial frames benefit from more relaxation time during the reference equilibrium trajectory, does not lead to less biased free energy estimations than protocol *R* (see PMFs (*gmx 3.1.4 - S - 133 traj*) or (*gmx 3.3.1 - S - 129 traj*) in Fig. 8 *a*). Only the less converged (*gmx 3.1.4 - S - 68 traj*) PMF could give this impression, but the fact that its initial frames are actually the 68 earliest (and least relaxed) of the (*gmx 3.1.4 - S - 133 traj*) data set invalidates the argument. As a whole, the comparison of *S* and *R* protocols seems to be in disfavor of the artifactual explanation of the potential energy drift. We finally note that, since the potential energy change is the same for the Tax and the P6A complexes, it cannot have an influence on the difference observed between the Tax and P6A PMFs.

The second and most likely explanation is the following. The above cumulant expansion results are subject to the strong hypothesis that the work distribution is Gaussian. The method in fact uses an extrapolation of this Gaussian distribution far in the lower tail. Indeed, from a work distribution centered at 380 kJ mol^{-1}, we try to estimate a ΔG of ~35 kJ mol^{-1}, which is approximately five standard deviations from the mean (Fig. 7). Although the Kolmogorov-Smirnov test confirms that the center of the work distribution is Gaussian, little can be said about the far tails. This issue is illustrated by an analytical example by Crooks and Jarzynski (90), where the work distribution has asymmetric tails although it is similar to a Gaussian in its center part. If in reality the lower tail of the actual work distribution for the TCR-pMHC system dies off more rapidly than a Gaussian, the free energy predicted by Eq. 30 would be an underestimation. In general, how far the tail needs to be extrapolated depends on the proportion of dissipative work performed, which in turn depends on the pulling speed and on the system considered. If the free energy barrier to overcome is high, it is likely that more dissipation is going to occur in a nonequilibrium crossing. This problem can be partly overcome with systems in which SMD trajectories can be made in the reverse direction as well. Work values from forward and reverse trajectories can be optimally combined in a method based on the Bennett acceptance ratio (91,92), which reduces the bias of the JI (note that in this case, only a free energy difference between two end states can be obtained, and not the full PMF). However, for a protein-protein system such as the TCR-pMHC, it is impossible to perform nonequilibrium binding simulations, since the final structures after fast docking would very unlikely correspond to the crystal structure of the complex. It was shown recently (93) that, in addition to barrier height, the complexity of the system and the number of degrees of freedom perpendicular to the reaction coordinate impact the accuracy of a PMF calculation with the Jarzynski method. If it is well known that large dissipative work is a crucial difficulty for the application of the Jarzynski method, then it is, on the other hand, impossible to estimate a priori what the average dissipative work would be for a given system and pulling speed. This is known only a posteriori, after the SMD simulations have been performed.

CONCLUSION

The primary interest of this study was of methodological nature. The Jarzynski method had never been applied to a protein-protein system of the size of the TCR-pMHC. An original pulling scheme called individual pulling was introduced, which allows us to prevent unrealistic molecular distortions and rotations during large protein-protein forced dissociation. Related to this, an appropriate postprocessing method was developed to unbias, smooth, and average the work profiles entering the JI. The height of the free energy barrier to overcome and the complexity of the TCR-pMHC system represent a challenge for the Jarzynski method. The obtained dissociation free energies largely underestimate experimental values, although the two-term cumulant expansion seems to converge with the number of trajectories available. Two explanations can be put forward. First, the energy drifts observed in the MD simulation could indicate that the system might not have reached perfect equilibrium before pulling, in which case residual relaxation would drive the PMF down. The second and most likely explanation pertains to the use of the second-order cumulant expansion to evaluate the exponential average in the JI. The extrapolation demanded outside of the observed work distribution seems excessive, due to the large amount of dissipative work generated. In those regions far from the mean, the tails of the true work distribution may differ significantly from a Gaussian (in our case the lower tail seems shorter than Gaussian). This appears to be a general caveat for the application of the Jarzynski method to large systems. However, the PMFs obtained with our SMD approach, although systematically biased with respect to experiment, are able to differentiate between the Tax and the P6A TCR-pMHC complexes, which differ only by a single point mutation.

For the particular system considered here, the A6 TCR in complex with the Tax peptide and the HLA-A2 MHC, understanding the drastic change in T cell response induced by a single mutation in the P6A peptide is biologically challenging. Looking at the steered unbinding simulations, no positional or energetic factor appeared to strongly correlate with the final work of a given trajectory, which emphasizes the complexity of the process. By averaging over all unbinding trajectories computed in this study, different energy contributions along the dissociation path can be monitored in a statistically meaningful way. For both Tax and P6A, the relative contribution of the peptide to the van der Waals interactions with the TCR is large, in line with the hydrophobic nature of the peptides. Conversely, the electrostatic interaction is dominated by the MHC, with a negligible contribution of the peptides. Moreover, we showed that the solvent plays an important role favoring the unbound state, both by resolvation of residues buried at the interface and by changing its average internal energy. The TCR-pMHC dissociation appears to be a complex molecular process with a large number of possible pathways involving a variety of simultaneous

interactions at the atomic level. A more biologically oriented study focusing on which specific residues or hydrogen bonds are critical for the observed high sensitivity to peptide mutation will be reported elsewhere (M. A. Cuendet, V. Zoete, and O. Michielin, in preparation).

We thank Vincent Zoete, Simon Bernèche, and Emanuele Paci for their useful comments.

We are grateful to the Vital-IT infrastructure of the Swiss Institute of Bioinformatics, the Hewlett-Packard Labs in Bristol, and the Cluster vs. Cancer Foundation for supplying the computing resources necessary for this work.

REFERENCES

1. Rudolph, M. G., R. L. Stanfield, and I. A. Wilson. 2006. How TCRs bind MHCs, peptides, and coreceptors. *Annu. Rev. Immunol.* 24:419–466.
2. Valmori, D., V. Dutoit, V. Schnuriger, A. L. Quiquerez, M. J. Pittet, P. Guillaume, V. Rubio-Godoy, P. R. Walker, D. Rimoldi, D. Liénard, J. C. Cerottini, P. Romero, and P. Y. Dietrich. 2002. Vaccination with a MelanA peptide selects an oligoclonal T cell population with increased functional avidity and tumor reactivity. *J. Immunol.* 168:4231–4240.
3. Dietrich, P. Y., F. A. L. Gal, V. Dutoit, M. J. Pittet, L. Trautman, A. Zippelius, I. Cognet, V. Widmer, P. R. Walker, O. Michielin, P. Guillaume, T. Connerotte, F. Jotereau, P. G. Coulie, P. Romero, J. C. Cerottini, M. Bonneville, and D. Valmori. 2003. Prevalent role of TCR α-chain in the selection of the preimmune repertoire specific for a human tumor-associated self-antigen. *J. Immunol.* 170:5103–5109.
4. Lyons, D. S., S. A. Lieberman, J. Hampl, J. J. Boniface, Y. Chien, L. J. Berg, and M. M. Davis. 1996. A TCR binds to antagonist ligands with lower affinities and faster dissociation rates than to agonists. *Immunity.* 5:53–61.
5. Rabinowitz, J. D., C. Beeson, D. S. Lyons, M. M. Davis, and H. M. McConnell. 1996. Kinetic discrimination in T-cell activation. *Proc. Natl. Acad. Sci. USA.* 93:1401–1405.
6. Hudrisier, D., B. Kessler, S. Valitutti, C. Horvath, J. C. Cerottini, and I. F. Luescher. 1998. The efficiency of antigen recognition by CD81 CTL clones is determined by the frequency of serial TCR engagement. *J. Immunol.* 161:553–562.
7. Rosette, C., G. Werlen, M. A. Daniels, P. O. Holman, S. M. Alam, P. J. Travers, N. R. J. Gascoigne, E. Palmer, and S. C. Jameson. 2001. The impact of duration versus extent of TCR occupancy on T cell activation, a revision of the kinetic proofreading model. *Immunity.* 15:59–70.
8. Schumacher, T. N. 2002. T-cell-receptor gene therapy. *Nat. Rev. Immunol.* 2:512–519.
9. Morgan, R. A., M. E. Dudley, J. R. Wunderlich, M. S. Hughes, J. C. Yang, R. M. Sherry, R. E. Royal, S. L. Topalian, U. S. Kammula, N. P. Restifo, Z. Zheng, A. Nahvi, C. R. de Vries, L. J. Rogers-Freezer, S. A. Mavroukakis, and S. A. Rosenberg. 2006. Cancer regression in patients after transfer of genetically engineered lymphocytes. *Science.* 314:126–129.
10. Chlewicki, L. K., P. D. Holler, B. C. Monti, M. R. Clutter, and D. M. Kranz. 2005. High-affinity, peptide-specific T cell receptors can be generated by mutations in CDR1, CDR2 or CDR3. *J. Mol. Biol.* 346:223–239.
11. Garboczi, D. N., P. Ghosh, U. Utz, Q. R. Fan, W. E. Biddison, and D. C. Wiley. 1996. Structure of the complex between human T-cell receptor, viral peptide and HLA-A2. *Nature.* 384:134–141.
12. Ding, Y. H., B. M. Baker, D. N. Garboczi, W. E. Biddison, and D. C. Wiley. 1999. Four A6-TCR/peptide/HLA-A2 structures that generate very different T cell signals are nearly identical. *Immunity.* 11:45–56.
13. Baker, B. M., S. J. Gagnon, W. E. Biddison, and D. C. Wiley. 2000. Conversion of a T cell antagonist into an agonist by repairing a defect in the TCR/peptide/MHC interface: implications for TCR signaling. *Immunity.* 13:475–484.
14. Baxter, T. K., S. J. Gagnon, R. L. Davis-Harrison, J. C. Beck, A. K. Binz, R. V. Turner, W. E. Biddison, and B. M. Baker. 2004. Strategic mutations in the class I major histocompatibility complex HLA-A2 independently affect both peptide binding and T cell receptor recognition. *J. Biol. Chem.* 279:29175–29184.
15. Davis-Harrison, R. L., K. M. Armstrong, and B. M. Baker. 2005. Two different T cell receptors use different thermodynamic strategies to recognize the same peptide/MHC ligand. *J. Mol. Biol.* 346:533–550.
16. Davis-Harrison, R. L., F. K. Insaidoo, and B. M. Baker. 2007. T Cell receptor binding transition states and recognition of peptide/MHC. *Biochemistry.* 46:1840–1850.
17. Armstrong, K. M., and B. M. Baker. 2007. A comprehensive calorimetric investigation of an entropically driven T cell receptor-peptide/major histocompatibility complex interaction. *Biophys. J.* 93:597–609.
18. Rudolph, M. G., J. G. Luz, and I. A. Wilson. 2002. Structural and thermodynamic correlates of T cell signaling. *Annu. Rev. Biophys. Biomol. Struct.* 31:121–149.
19. Lanzavecchia, A., G. Lezzi, and A. Viola. 1999. From TCR engagement to T cell activation: a kinetic view of T cell behavior. *Cell.* 96: 1–4.
20. Michielin, O., and M. Karplus. 2002. Binding free energy differences in a TCR-peptide-MHC complex induced by a peptide mutation: a simulation analysis. *J. Mol. Biol.* 324:547–569.
21. Schlitter, J., M. Engels, P. Krüger, E. Jacoby, and A. Wollmer. 1993. Targeted molecular dynamics simulation of conformational change—application to the TR transition in insulin. *Mol. Simul.* 10:291–308.
22. Grubmüller, H., B. Heymann, and P. Tavan. 1996. Ligand binding: molecular mechanics calculation of the streptavidin-biotin rupture force. *Science.* 271:997–999.
23. Hummer, G., and A. Szabo. 2001. Free energy reconstruction from nonequilibrium single-molecule pulling experiments. *Proc. Natl. Acad. Sci. USA.* 98:3658–3661.
24. Park, S., and K. Schulten. 2004. Calculating potentials of mean force from steered molecular dynamics information. *J. Chem. Phys.* 120: 5946–5961.
25. Schurr, J. M., and B. S. Fujimoto. 2003. Equalities for the nonequilibrium work transferred from an external potential to a molecular system. Analysis of single-molecule extension experiments. *J. Phys. Chem. B.* 107:14007–14019.
26. Isralewitz, B., J. Baudry, J. Gullingsrud, D. Kosztin, and K. Schulten. 2001. Steered molecular dynamics investigations of protein function. *J. Mol. Graph. Model.* 19:13.
27. Rief, M., and H. Grubmüller. 2002. Force spectroscopy of single biomolecules. *ChemPhysChem.* 3:255–266.
28. Lu, H., B. Isralewitz, A. Krammer, V. Vogel, and K. Schulten. 1998. Unfolding of titin immunoglobulin domains by steered molecular dynamics simulation. *Biophys. J.* 75:662–671.
29. Bayas, M. V., K. Schulten, and D. Leckband. 2003. Forced detachment of the CD2–CD58 complex. *Biophys. J.* 84:2223–2233.
30. Jarzynski, C. 1997. A nonequilibrium equality for free energy differences. *Phys. Rev. Lett.* 78:2690–2693.
31. Zuckerman, D. M., and T. B. Woolf. 2004. Systematic finite-sampling inaccuracy in free energy differences and other nonlinear quantities. *J. Stat. Phys.* 114:1303–1323.
32. Oberhofer, H., C. Dellago, and P. L. Geissler. 2005. Biased sampling of nonequilibrium trajectories: can fast switching simulations outperform conventional free energy calculation methods? *J. Phys. Chem. B.* 109:6902–6915.
33. Shirts, M. R., and V. S. Pande. 2005. Comparison of efficiency and bias of free energies computed by exponential averaging, the Bennett acceptance ratio, and thermodynamic integration. *J. Chem. Phys.* 122:144107–144116.

34. Ytreberg, F. M., R. H. Swendsen, and D. M. Zuckerman. 2006. Comparison of free energy methods for molecular systems. *J. Chem. Phys.* 125:184114–184124.
35. Jarzynski, C. 1997. Equilibrium free energy differences from nonequilibrium measurements: a master equation approach. *Phys. Rev. E Stat. Phys. Plasmas Fluids Relat. Interdiscip. Topics.* 56:5018–5035.
36. Crooks, G. E. 1999. Entropy production fluctuation theorem and the nonequilibrium work relation for free energy differences. *Phys. Rev. E Stat. Phys. Plasmas Fluids Relat. Interdiscip. Topics.* 60:2721–2726.
37. Evans, D. J., and D. J. Searles. 2002. The fluctuation theorem. *Adv. Phys.* 51:1529–1585.
38. Jarzynski, C. 2000. Hamiltonian derivation of a detailed fluctuation theorem. *J. Stat. Phys.* 98:77–102.
39. Evans, D. J. 2003. A nonequilibrium free energy theorem for deterministic systems. *Mol. Phys.* 101:1551–1553.
40. Cuendet, M. A. 2006. Statistical mechanical derivation of Jarzynski's identity for thermostated non-Hamiltonian dynamics. *Phys. Rev. Lett.* 96:120602.
41. Cuendet, M. A. 2006. The Jarzynski identity derived for general non-Hamiltonian and Hamiltonian dynamics generating the NVT or NPT ensembles. *J. Chem. Phys.* 125:144109.
42. Scholl-Paschinger, E., and C. Dellago. 2006. A proof of Jarzynski's non-equilibrium work theorem for dynamical systems that conserve the canonical distribution. *J. Chem. Phys.* 125:054105.
43. Liphardt, J., S. Dumont, S. B. Smith, I. Tinoco, Jr., and C. Bustamente. 2002. Equilibrium information from nonequilibrium measurements in an experimental test of Jarzynski's identity. *Science.* 296:1832–1835.
44. Jensen, M. O., S. Park, E. Tajkhorshid, and K. Schulten. 2002. Energetics of glycerol conduction through aquaglyceroporin GlpF. *Proc. Natl. Acad. Sci. USA.* 99:6731–6376.
45. Park, S., F. Khalili-Araghi, E. Tajkhorshid, and K. Schulten. 2003. Free energy calculation from steered molecular dynamics simulations using Jarzynski's equality. *J. Chem. Phys.* 119:3559–3566.
46. Xiong, H., A. Crespo, M. Marti, D. Estrin, and A. E. Roitberg. 2006. Free energy calculations with non-equilibrium methods: applications of the Jarzynski relationship. *Theor. Chem. Acc.* 116:338–346.
47. Zhang, D., J. Gullingsrud, and J. A. McCammon. 2006. Potentials of mean force for acetylcholine unbinding from the α7 nicotinic acetylcholine receptor ligand-binding domain. *J. Am. Chem. Soc.* 128:3019–3026.
48. Reference deleted in proof.
49. Cebecauer, M., P. Guillaume, S. Mark, O. Michielin, N. Boucheron, M. Bezard, B. H. Meye, J. M. Segura, H. Vogel, and I. F. Luescher. 2005. CD^{8+} cytotoxic T lymphocytes activation by soluble major histocompatibility complex (MHC)-peptide dimers. *J. Biol. Chem.* 280:23820–23828.
50. Kjer-Nielsen, L., C. S. Clements, A. W. Purcell, A. G. Brooks, J. C. Whisstock, S. R. Burrows, J. McCluskey, and J. Rossjohn. 2003. A structural basis for the selection of dominant $\alpha\beta$ T cell receptors in antiviral immunity. *Immunity.* 18:53–64.
51. van Gunsteren, W. F., T. C. Beutler, F. Fraternali, P. M. King, A. E. Mark, and P. E. Smith. 1993. Computation of free energy in practice: choice of approximations and accuracy limiting factors. *In* Computer Simulation of Biomolecular Systems, Theoretical and Experimental Applications, Vol. 2. W. F. van Gunsteren, P. K. Weiner, and A. J. Wilkinson, editors. Escom Science Publishers, Leiden, The Netherlands.
52. Ferrenberg, A. M., and R. H. Swendsen. 1989. Optimized Monte Carlo data analysis. *Phys. Rev. Lett.* 63:1195–1198.
53. Kumar, S., D. Bouzida, R. H. Swendsen, P. A. Kollman, and J. M. Rosenberg. 1992. The weighted histogram analysis method for free-energy calculations on biomolecules. I. The method. *J. Comput. Chem.* 13:1011–1021.
54. Gullingsrud, J. R., R. Braun, and K. Schulten. 1999. Reconstructing potentials of mean force through time series analysis of steered molecular dynamics simulations. *J. Comput. Phys.* 151:190–211.
55. Hummer, G., and A. Szabo. 2005. Free energy surfaces from single-molecule force spectroscopy. *Acc. Chem. Res.* 38:504–513.
56. Jarzynski, C. 2006. Rare events and the convergence of exponentially averaged work values. *Phys. Rev. E Stat. Nonlin. Soft Matter Phys.* 73:046105–046110.
57. Hendrix, D. A., and C. Jarzynski. 2001. A ''fast growth'' method of computing free energy differences. *J. Chem. Phys.* 114:5974–5981.
58. Ytreberg, F. M., and D. M. Zuckerman. 2004. Efficient use of nonequilibrium measurement to estimate free energy differences for molecular systems. *J. Comput. Chem.* 25:1749–1759.
59. Sun, S. X. 2003. Equilibrium free energies from path sampling of nonequilibrium trajectories. *J. Chem. Phys.* 118:5769–5775.
60. Ytreberg, F. M., and D. M. Zuckerman. 2004. Single-ensemble nonequilibrium path-sampling estimates of free energy differences. *J. Chem. Phys.* 120:10876.
61. Roux, B. 1995. The calculation of the potential of mean force using computer simulations. *Comput. Phys. Commun.* 91:275–282.
62. Torrie, G. M., and J. P. Valleau. 1977. Nonphysical sampling distributions in Monte Carlo free-energy estimation: umbrella sampling. *J. Comput. Phys.* 23:187–199.
63. Hummer, G. 2001. Fast-growth thermodynamic integration: error and efficiency analysis. *J. Chem. Phys.* 114:7330–7339.
64. Marcinkiewicz, J. 1939. On a property of Gauss's law. *Math. Z.* 44: 612–618.
65. Hermans, J. 1991. Simple analysis of noise and hysteresis in (slow-growth) free energy simulations. *J. Phys. Chem.* 95:9029–9032.
66. Reiser, J. B., C. Darnault, C. Grégoire, T. Mosser, G. Mazza, A. Kearney, P. A. van der Merwe, J. C. Fontecilla-Camps, D. Housset, and B. Malissen. 2003. CDR3 loop flexibility contributes to the degeneracy of TCR recognition. *Nat. Immunol.* 4:241–247.
67. van Gunsteren, W. F., S. R. Billeter, A. A. Eising, P. H. Hünenberger, P. Krüger, A. E. Mark, W. R. P. Scott, and I. G. Tironi. 1996. Biomolecular Simulation: The GROMOS96 Manual and User Guide. Vdf Hochschulverlag AG an der ETH Zürich, Zürich, Switzerland.
68. Miyamoto, S., and P. A. Kollman. 1992. SETTLE: an analytical version of the SHAKE and RATTLE algorithms for rigid water models. *J. Comput. Chem.* 13:952–962.
69. Berendsen, H. J. C., J. P. M. Postma, W. F. van Gunsteren, and J. Hermans. 1981. Intermolecular Forces. Reidel, Dordrecht.
70. Petrone, P. M., and A. E. Garcia. 2004. MHC-peptide binding is assisted by bound water molecules. *J. Mol. Biol.* 338:419–435.
71. Essmann, U., L. Perera, M. L. Berkowitz, T. Darden, H. Lee, and L. G. Pedersen. 1995. A smooth particle mesh Ewald method. *J. Chem. Phys.* 103:8577–8592.
72. Hess, B., H. Bekker, H. J. C. Berendsen, and J. G. E. M. Fraaije. 1997. LINCS: a linear constraint solver for molecular simulations. *J. Comput. Chem.* 18:1463–1472.
73. Ryckaert, J. P., G. Ciccotti, and H. J. C. Berendsen. 1977. Numerical integration of the Cartesian equations of motion of a system with constraints: molecular dynamics of *n*-alkanes. *J. Comput. Phys.* 23: 327–341.
74. Hoover, W. G. 1985. Canonical dynamics: equilibrium phase-space distributions. *Phys. Rev. A.* 31:1695–1697.
75. Parrinello, M., and A. Rahman. 1981. Polymorphic transitions in single crystals: a new molecular dynamics method. *J. Appl. Phys.* 52:7182–7190.
76. Nosé, S., and M. L. Klein. 1983. Constant pressure molecular dynamics for molecular systems. *Mol. Phys.* 50:1055–1076.
77. Caves, L. S. D., J. D. Evanseck, and M. Karplus. 1998. Locally accessible conformations of proteins: multiple molecular dynamics simulations of crambin. *Protein Sci.* 7:649–666.
78. Berendsen, H. J. C., D. van der Spoel, and R. van Drunen. 1995. GROMACS: a message-passing parallel molecular dynamics implementation. *Comput. Phys. Commun.* 91:43–56.

79. Lindahl, E., B. Hess, and D. van der Spoel. 2001. GROMACS 3.0: a package for molecular simulation and trajectory analysis. *J. Mol. Model.* 7:306–317.

80. van der Spoel, D., E. Lindahl, B. Hess, G. Groenhof, A. E. Mark, and H. J. C. Berendsen. 2005. GROMACS: fast, flexible, and free. *J. Comput. Chem.* 26:1701–1718.

81. Cuendet, M. A., and W. F. van Gunsteren. 2007. On the calculation of velocity-dependent properties in molecular dynamics simulations using the leap-frog integration algorithm. *J. Chem. Phys.* 127: 184102.

82. Zoete, V., and O. Michielin. 2007. Comparison between computational alanine scanning and per-residue binding free energy decomposition for protein-protein association using MM-GBSA: application to the TCR-p-MHC complex. *Proteins.* 67:1026–1047.

83. Tironi, I., R. Sperb, P. Smith, and W. van Gunsteren. 1995. A generalized reaction field method for molecular dynamics simulations. *J. Chem. Phys.* 102:5441–5459.

84. Luo, H., and K. Sharp. 2002. On the calculation of absolute macromolecular binding free energies. *Proc. Natl. Acad. Sci. USA.* 99: 10399–10404.

85. Swanson, J. M., R. H. Henchman, and J. A. McCammon. 2004. Revisiting free energy calculations: a theoretical connection to MM/PBSA and direct calculation of the association free energy. *Biophys. J.* 86:67–74.

86. Boresch, S., F. Tettinger, and M. Leitgeb. 2003. Absolute binding free energies: a quantitative approach for their calculation. *J. Phys. Chem. B.* 107:9535–9551.

87. Woo, H.-J., and B. Roux. 2005. Calculation of absolute protein-ligand binding free energy from computer simulations. *Proc. Natl. Acad. Sci. USA.* 102:6825–6830.

88. Hünenberger, P. H., and J. A. McCammon. 1999. Ewald artifacts in computer simulations of ionic solvation and ion–ion interaction: a continuum electrostatics study. *J. Chem. Phys.* 110:1856–1872.

89. Kastenholz, M. A., and P. H. Hünenberger. 2004. Influence of artificial periodicity and ionic strength in molecular dynamics simulations of charged biomolecules employing lattice-sum methods. *J. Phys. Chem. B.* 108:774–788.

90. Crooks, G. E., and C. Jarzynski. 2007. Work distribution for the adiabatic compression of a dilute and interacting classical gas. *Phys. Rev. E Stat. Nonlin. Soft Matter Phys.* 75:021116.

91. Crooks, G. E. 2000. Path-ensemble averages in systems driven far from equilibrium. *Phys. Rev. E Stat. Phys. Plasmas Fluids Relat. Interdiscip. Topics.* 61:2361–2366.

92. Shirts, R., E. Bair, G. Hooker, and V. S. Pande. 2003. Equilibrium free energies from nonequilibrium measurements using maximum-likelihood methods. *Phys. Rev. Lett.* 91:140601.

93. Baştuğ, T., and S. Kuyucak. 2007. Application of Jarzynski's equality in simple versus complex systems. *Chem. Phys. Lett.* 436:383–387.